

Magnon Transport in Quasi-Two-Dimensional van der Waals AntiferromagnetsWenyu Xing,^{1,2} Luyi Qiu,^{1,2} Xirui Wang,^{1,2} Yunyan Yao,^{1,2} Yang Ma,^{1,2}
Ranran Cai,^{1,2} Shuang Jia,^{1,2,3} X. C. Xie,^{1,2,3} and Wei Han^{1,2,*}¹*International Center for Quantum Materials, School of Physics, Peking University,
Beijing 100871, Peoples Republic of China*²*Collaborative Innovation Center of Quantum Matter, Beijing 100871, Peoples Republic of China*³*CAS Center for Excellence in Topological Quantum Computation,
University of Chinese Academy of Sciences, Beijing 100190, Peoples Republic of China*

(Received 22 August 2018; revised manuscript received 12 December 2018; published 7 February 2019)

The recent emergence of 2D van der Waals magnets down to atomic-layer thickness provides an exciting platform for exploring quantum magnetism and spintronics applications. The van der Waals nature stabilizes the long-range ferromagnetic order as a result of magnetic anisotropy. Furthermore, giant tunneling magnetoresistance and electrical control of magnetism have been reported. However, the potential of 2D van der Waals magnets for magnonics, magnon-based spintronics, has not been explored yet. Here, we report the experimental observation of long-distance magnon transport in quasi-two-dimensional van der Waals antiferromagnet MnPS₃, which demonstrates the 2D magnets as promising material candidates for magnonics. As the 2D MnPS₃ thickness decreases, a shorter magnon diffusion length is observed, which could be attributed to the surface-impurity-induced magnon scattering. Our results could pave the way for exploring quantum magnonics phenomena and designing future magnonics devices based on 2D van der Waals magnets.

DOI: [10.1103/PhysRevX.9.011026](https://doi.org/10.1103/PhysRevX.9.011026)Subject Areas: Condensed Matter Physics,
Materials Science, Spintronics**I. INTRODUCTION**

The recent emergence of two-dimensional (2D) van der Waals magnets down to atomic-layer thickness has attracted considerable interest and provided an exciting platform for exploring new physical phenomena in low-dimensional magnetism [1–15]. The long-range ferromagnetic order in 2D magnets has been demonstrated in bilayer Cr₂Ge₂Te₆ and single-layer CrI₃ as a result of magnetic anisotropy [1,2,16]. Shortly, the potential of such van der Waals magnets for spintronics applications has been intensively explored. For example, giant tunneling magnetoresistance in bilayer CrI₃ has been demonstrated [17–19], which is much higher compared to conventional single-crystalline-MgO barrier-based ferromagnetic tunneling junctions [20,21]. The important role of magnon-assistant tunneling through thin CrBr₃ barriers has been shown in the graphene/CrBr₃/graphene heterostructures [22]. Because of their 2D nature, efficient electrical control of magnetism in 2D ferromagnetic materials has also been

explored [3,23–26], which provides an alternative route towards high-temperature ferromagnetic semiconductors [27,28]. Furthermore, room-temperature 2D ferromagnetism in monolayer van der Waals magnet has also been demonstrated in epitaxial films and ionic liquid gated flakes [8,9,25].

Magnonics refers to the magnon-based spintronics, the use of magnon-mediated spin current for information logic and computing applications [29]. One of the major research directions is to search the suitable magnon transport channel materials, which can propagate magnons over a long distance. Recently, the long-distance magnon transport has been demonstrated in 3D ferromagnetic and antiferromagnetic insulators, such as YIG, Cr₂O₃, and Fe₂O₃ [30–32]. Specially, antiferromagnetic Fe₂O₃ offers an electrically tunable magnon channel that could be used for magnonics devices that could operate in the absence of any magnetic field [32]. Different from 3D magnetic insulators, such 2D van der Waals magnets offer special platforms for very intriguing quantum transport phenomena, including the spin Nernst effect, topological and Weyl magnons that have already been intensively studied theoretically [33–35]. However, the potential of 2D van der Waals magnets for magnon transport has not been experimentally investigated yet.

Here, we report the magnon transport properties in 2D van der Waals antiferromagnet MnPS₃. The long-distance

*weihan@pku.edu.cn

Published by the American Physical Society under the terms of the [Creative Commons Attribution 4.0 International license](https://creativecommons.org/licenses/by/4.0/). Further distribution of this work must maintain attribution to the author(s) and the published article's title, journal citation, and DOI.

magnon propagation over several micrometers in 2D MnPS₃ has been demonstrated, which is comparable to the 3D ferromagnetic insulator yttrium iron garnet (YIG). Systematical studies on the spacing dependence of the nonlocal magnon signal reveal a magnon relaxation length of several micrometers. As the temperature decreases, a longer magnon relaxation length is observed, which could be related to longer magnon lifetimes in such a van der Waals antiferromagnet at lower temperatures. As the 2D MnPS₃ thickness decreases, a shorter magnon diffusion length is observed, which could be attributed to the surface-impurity-induced magnon scattering. These experimental results have demonstrated 2D van der Waals magnets as a new platform for the magnonics applications [29,36], and could further pave the way for exploring magnon-dependent quantum transport phenomena in 2D van der Waals magnets [33–35,37].

II. EXPERIMENTAL

Figure 1(a) illustrates the magnon transport in the quasi-2D van der Waals antiferromagnet MnPS₃ devices, where the 2D MnPS₃ flakes are prepared on the ~300 nm SiO₂/Si substrates from bulk MnPS₃ single crystals using the mechanical exfoliation method [23]. Bulk MnPS₃ single crystals are grown using the chemical vapor transport method. Stoichiometric amounts of high-purity manganese, red phosphorus, and sulfur were sealed into an evacuated quartz tube in a temperature gradient from 780 °C (source region) to 730 °C (growth region) for seven days. Figure 1(b) shows the crystalline and spin structures of the van der Waals antiferromagnet MnPS₃. In each layer of the crystal's *ab* plane, the spins of the Mn atoms are antiferromagnetic coupled with their nearest neighbors, while the interlayer exchange coupling between the Mn spins is ferromagnetic [38]. The Néel temperature (T_N) of MnPS₃ bulk single crystals is ~79 K, obtained from temperature-dependent magnetization measurement (Supplemental Material, Fig. S1 [39]) under the magnetic fields parallel and perpendicular to the crystal's *ab* plane in a Magnetic Properties Measurement System (MPMS; Quantum Design).

The prepared 2D MnPS₃ flakes on ~300 nm SiO₂/Si substrates are first identified by a Nikon high-resolution optical microscope, and then fabricated for the nonlocal magnon devices using standard electron-beam lithography and lift-off processes. The electrodes are made of 10-nm-thick Pt grown in a magnetron sputtering system with a base pressure lower than 8×10^{-7} mbar. The width of the Pt electrodes is ~200 nm. Figure 1(c) shows the optical image of a typical magnon device made on 8-nm 2D MnPS₃ flake, where the thickness is determined by atomic force microscopy (Supplemental Material, Fig. S2 [39]). Raman studies show that the electron-beam lithography and device fabrication processes are not damaging the MnPS₃ flakes (Supplemental Material, Fig. S3 [39]).

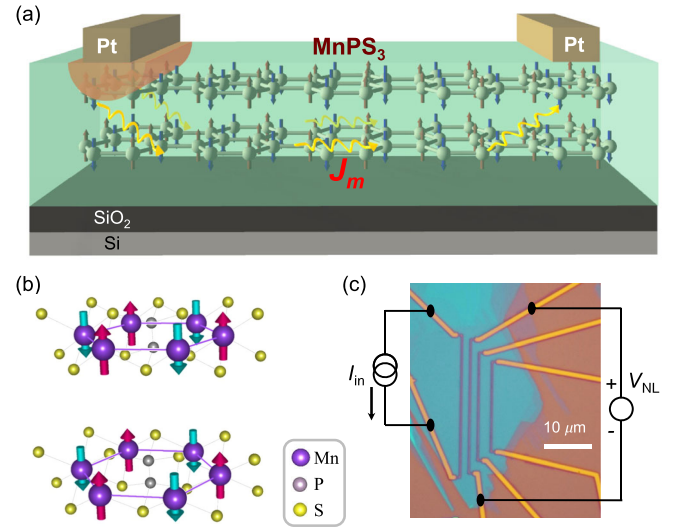


FIG. 1. Illustration of magnon transport in quasi-2D antiferromagnet MnPS₃ devices. (a) Schematic of magnon transport in the quasi-2D MnPS₃. J_m represents the magnon-mediated spin current. The left Pt electrode is used as magnon injector via thermal spin injection, and the right Pt electrode is used as magnon detector via inverse spin Hall effect. (b) The crystal and spin structures of van der Waals antiferromagnet MnPS₃. (c) Schematic of nonlocal measurement on a typical MnPS₃ device via the low-frequency lock-in technique. The thickness of the MnPS₃ flake is 8 nm determined via atomic force microscopy (Supplemental Material, Fig. S2 [39]).

The magnon transport in the quasi-2D van der Waals antiferromagnet MnPS₃ is measured using the nonlocal geometry via standard low-frequency lock-in technique in a Physical Properties Measurement System (PPMS; Quantum Design). During the nonlocal magnon transport measurement, a current source (Keithley K6221) is used to provide the low-frequency ac current ($f = 7$ Hz) in the range from 10 to 150 μ A in the spin injector Pt electrode, and the nonlocal voltages are measured using lock-in amplifiers (Stanford Research SR830). The voltage probes the magnon-dependent chemical potential due to magnon diffusion in the quasi-2D MnPS₃ channel. During the measurement, low noise voltage preamplifiers (Stanford Research SR560) are used to enhance the signal-to-noise ratio.

The magnons are generated in quasi-2D van der Waals antiferromagnet MnPS₃ under the left Pt electrode (magnon injector), and then diffuse towards the right Pt electrode (magnon detector) which detects the magnon-mediated spin current via inverse spin Hall effect of Pt in the nonlocal geometry [30–32,40,41]. To perform magnon injection, both electrical means via spin Hall effect of Pt and thermal means via thermal spin injection could be utilized [30], which give rise to the first and second harmonic nonlocal voltages probed at the magnon detector ($V_{1\omega}$ and $V_{2\omega}$), respectively. Both means could be used to investigate the magnon transport properties in magnetic

insulators, as demonstrated in previous reports [41–44]. In our experiment with the ac injection current [I_{in} in Fig. 1(c)] in the range from 10 to 150 μA , only the second harmonic nonlocal voltages could be clearly observed, while no obvious first harmonic voltages could be detected (Supplemental Material, Fig. S4 [39]). This result could be attributed to higher-efficiency magnon generation via thermal heating than that via the electrical means due to spin Hall effect of Pt. Hence, to probe the magnon transport in quasi-2D van der Waals MnPS_3 , thermal means is utilized to generate the magnons arising from the temperature gradient at the MnPS_3 -Pt interface via Joule heating [30,31,42,45].

III. RESULTS AND DISCUSSION

Figure 2(a) shows the nonlocal magnon transport and measurement geometry in MnPS_3 , and Fig. 2(b) shows the second harmonic resistance ($R_{2\omega} = \sqrt{2}V_{2\omega}/I_{\text{in}}^2$) as a function of the magnetic field angle (φ) measured on the nonlocal magnon devices of 8-nm (black) and 16-nm (blue) MnPS_3 flakes, with spacing (d) of 2 μm for both devices measured at $T = 2$ K. During the measurement, the

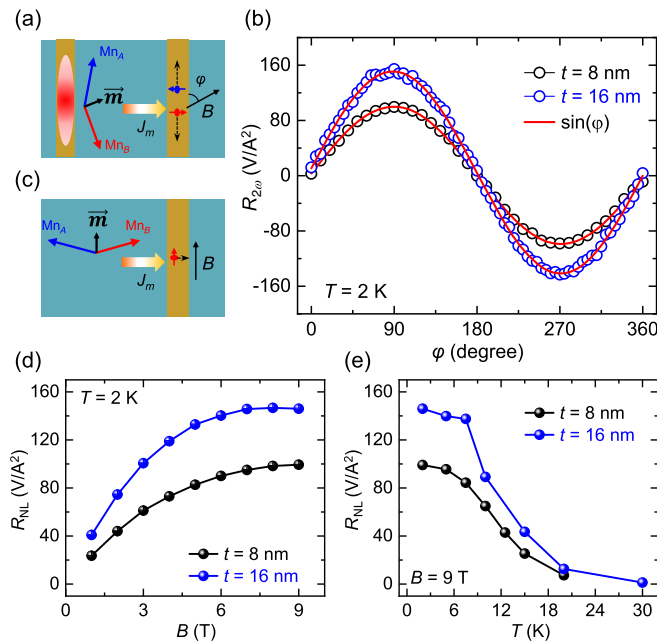


FIG. 2. Nonlocal magnon transport measurements in quasi-2D antiferromagnet MnPS_3 . (a) Schematic of the generation, transport, and detection of magnon-mediated spin current in MnPS_3 magnon devices. (b) The nonlocal resistances of the 8-nm and 16-nm MnPS_3 devices ($d = 2 \mu\text{m}$) as a function of the in-plane magnetic field angle at $T = 2$ K and $B = 9$ T. (c) Illustration of the zero voltage signal when the magnetic field angle is 0° . (d) The in-plane magnetic field dependence of the nonlocal magnon signal for both MnPS_3 devices at $T = 2$ K. (e) The temperature dependence of the nonlocal magnon signal for both MnPS_3 devices at $B = 9$ T.

in-plane static magnetic field (B) is held at 9 T, which gives rise to a canted magnetic moment (\vec{m}) between Mn_A and Mn_B in different magnetic sublattices [Fig. 2(a)]. The magnon-mediated spin current (J_m) carrying the angular momentum parallel to \vec{m} will be converted to the electron-mediated spin current in Pt. Thus, the spin accumulation direction is parallel to \vec{m} . When the magnetic field angle is 90° (-90°), the maximum (minimum) voltages will be detected. On the other hand, if the magnetic field angle is 0° , as illustrated in Fig. 2(c), zero voltage signal is detected via inverse spin Hall effect since the spin accumulation direction is parallel to the Pt electrode. The 2D MnPS_3 magnon devices are rotated from 0° to 360° in an in-plane static magnetic field, leading to the 2π -periodic rotation of \vec{m} . No clear signals of first harmonic nonlocal voltage could be detected under the ac injection current from 10 to 150 μA , which could be attributed to lower efficiency of magnon generation via the electrical means compared to the thermal means (Supplemental Material, Fig. S4 [39]). This observation is in accordance with previous reports on ferromagnetic insulator YIG and antiferromagnetic insulator Cr_2O_3 [30,31,45]. Consistent with expectations for the transport of incoherent magnons [30,31], the second harmonic nonlocal voltage scales quadratically with the injection current (Supplemental Material, Fig. S5 [39]).

Since the 2D MnPS_3 is insulating (Supplemental Material, Figs. S6 and S7 [39]), the flow of any charge current in the 2D MnPS_3 is forbidden, which rules out any nonlocal voltage arising from charge current leakage in the MnPS_3 channel. Furthermore, the absence of the $R_{2\omega}$ signal in the control samples fabricated directly on the SiO_2/Si substrates confirms that the $R_{2\omega}$ signal can only be obtained on the MnPS_3 devices via magnon transport (Supplemental Material, Fig. S8 [39]).

As discussed earlier, since the magnons are injected via thermal means and the diffusive magnons are detected via the inverse spin Hall effect of Pt, $R_{2\omega}$ is expected to be proportional to $\sin(\varphi)$ [30]:

$$R_{2\omega} = R_{\text{NL}} \sin(\varphi), \quad (1)$$

where the R_{NL} is the nonlocal spin signal. The red solid lines in Fig. 2(b) are best-fitting curves based on Eq. (1), from which R_{NL} is determined to be 99 V/A^2 for the 8-nm MnPS_3 device and 146 V/A^2 for the 16-nm MnPS_3 device, respectively. Obviously, a larger nonlocal magnon signal (R_{NL}) is observed for 16-nm MnPS_3 device, which could be attributed to longer magnon relaxation lengths for thicker MnPS_3 and be discussed later in detail. The in-plane magnetic field dependence of the nonlocal magnon signals on both devices is shown in Fig. 2(d) ($T = 2$ K). As in-plane magnetic field increases, the canted magnetic moment increases, giving rise to the enhancement of the second harmonic nonlocal magnon signals [31]. Figure 2(e) shows the temperature dependence of the nonlocal magnon

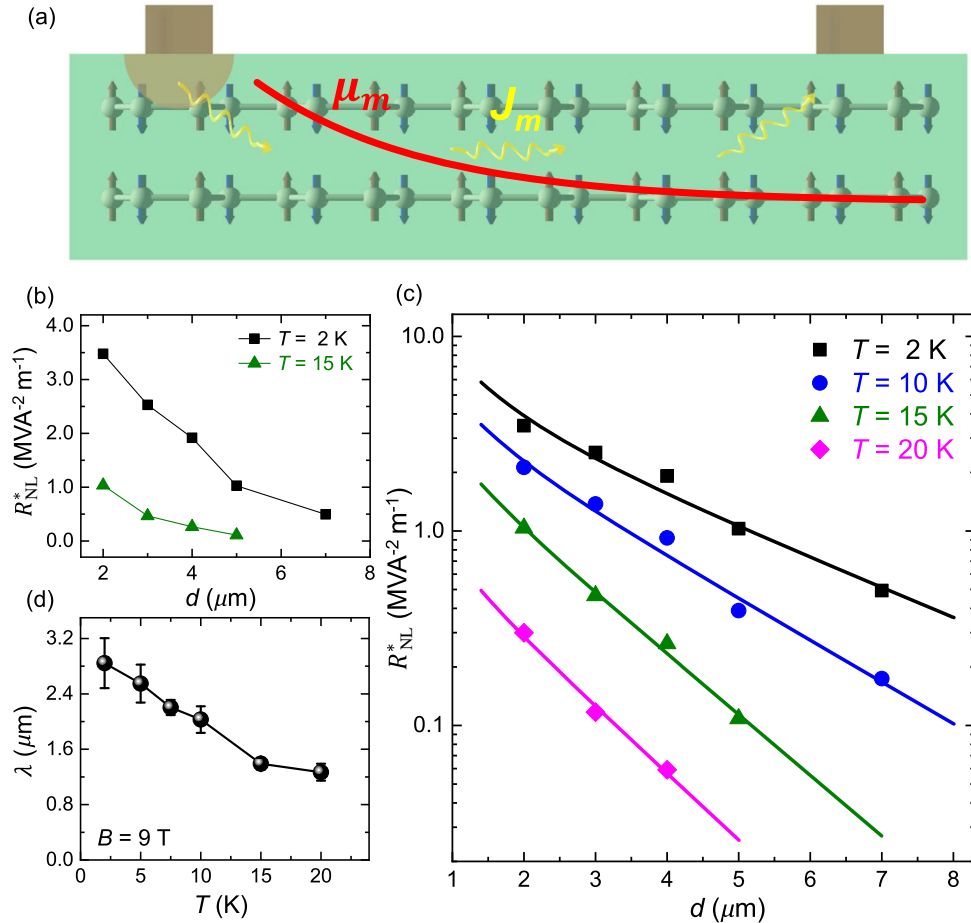


FIG. 3. The measurement of magnonic properties in quasi-2D antiferromagnet MnPS₃. (a) Schematic of the exponential decay (solid red line) of magnon-dependent chemical potential (μ_m) during the flow of magnon-mediated spin current (J_m). For simplicity, the magnon depletion below the Pt injector is not shown here (see Supplemental Material, Fig. S9 for details). (b) The spacing (d) dependence of the normalized nonlocal spin signals (R_{NL}^*) of the 16-nm MnPS₃ device measured at $T = 2$ and 15 K. (c) The spacing (d) dependence of the normalized nonlocal spin signals (R_{NL}^*). The solid lines represent the best-fitting results based on Eq. (3). (d) The temperature dependence of the magnon relaxation length for the 16-nm MnPS₃ device.

signals of both devices at $B = 9$ T. The nonlocal magnon signals are observed when the temperature is lower than ~ 20 K for the 8-nm MnPS₃ device and ~ 30 K for the 16-nm MnPS₃ device, which could be attributed to lower Néel temperature for thinner MnPS₃, a Heisenberg antiferromagnet [46]. These results demonstrate the potential of using a quasi-2D van der Waals antiferromagnet for the magnon transport, which might have advantages compared to ferromagnetic insulator YIG, such as the capability of functioning in the presence of large magnetic fields and the absence of stray fields [47,48].

To investigate the magnon transport properties of quasi-2D van der Waals antiferromagnet MnPS₃, the spacing profile of the magnon-dependent chemical potential (μ_m) is systematically studied. Since the MnPS₃ thickness is much smaller than the spacing between the two Pt electrodes, magnon transport is expected to follow the one-dimensional drift-diffusion model [30,49]. As illustrated in Fig. 3(a), μ_m is expected to exponentially decay as

the magnon-mediated spin current diffuses away from the magnon injector in the presence of magnon scatterings. At the distance of d away from the magnon injector, μ_m can be described by the following expression:

$$\mu_m = \frac{\mu_0}{\lambda} \frac{\exp(\frac{d}{\lambda})}{1 - \exp(\frac{2d}{\lambda})}, \quad (2)$$

where μ_0 is the magnon-dependent chemical potential in MnPS₃ under the Pt injector and λ is the magnon relaxation length. Quantitatively, the decrease of the nonlocal magnon resistances as a function of d can be expressed by [41,42]

$$R_{NL} = \frac{C}{\lambda} \frac{\exp(\frac{d}{\lambda})}{1 - \exp(\frac{2d}{\lambda})}, \quad (3)$$

where C is a constant related to the spin-to-charge conversion efficiency of Pt, the magnon injection-detection

efficiencies, and the spin-mixing conductances at the interface between MnPS_3 and Pt.

Figure 3(b) shows the normalized nonlocal magnon resistance (R_{NL}^*) as a function of d for the 16-nm MnPS_3 device measured at $B = 9$ T and $T = 2$ and 15 K, respectively. R_{NL}^* is used to take into account of the length effect of the magnon detector, and it is calculated using the following formula: $R_{\text{NL}}^* = R_{\text{NL}}(1/l_{\text{Pt},D})$, where $l_{\text{Pt},D}$ is the length of the magnon detector. During the investigation of the magnon relaxation lengths, the spacings are purposely chosen to be longer than or equal to $2 \mu\text{m}$, since there is a magnetic depletion region close to the Pt injector arising from local Joule heating induced spin Seebeck effect (Supplemental Material, Fig. S9) [43]. The spin signal probed from the local Pt injector is of opposite sign compared to the nonlocal Pt detector which probes the magnon transport across a spacing that is much bigger than the thickness of MnPS_3 (Supplemental Material, Fig. S9 [39]).

To quantitatively determine the magnon relaxation length, the $\log(R_{\text{NL}}^*)$ vs d measured at various temperatures are plotted in Fig. 3(c). It is clear that the experimental results at various temperatures are all in good agreement with the exponential decay of magnon-dependent chemical potential expected theoretically [solid lines in Fig. 3(c)]. Based on the best-fitting results of the experimental data, the magnon relaxation lengths of the 16-nm MnPS_3 are obtained to be $2.8 \pm 0.4 \mu\text{m}$ at $T = 2$ K, $2.0 \pm 0.2 \mu\text{m}$ at $T = 10$ K, $1.4 \pm 0.1 \mu\text{m}$ at $T = 15$ K, and $1.3 \pm 0.1 \mu\text{m}$ at $T = 20$ K, respectively. As shown in Fig. 3(d), the magnon relaxation length increases as temperature decreases, which could be attributed to the enhancement of the magnon lifetime at lower temperatures. This observation is consistent with previous reports of enhancement of magnon lifetimes at low temperatures in antiferromagnets $\text{Cu}_2\text{V}_2\text{O}_7$ and MnF_2 investigated via spin Seebeck-effect measurements [50,51].

Next, the magnon transport and relaxation properties of quasi-2D MnPS_3 are investigated as a function of the MnPS_3 thickness. For this purpose, various magnon devices are fabricated on MnPS_3 flakes with different thicknesses and the magnon relaxation length is obtained via the spacing dependence of the nonlocal spin signal. The exponential decay of magnon-dependent chemical potential has been observed on all the MnPS_3 devices, which has been further confirmed on the MnPS_3 devices with much larger spacings (Supplemental Material, Fig. S10 [39]). Figures 4(a) and 4(b) show the temperature dependence of the magnon relaxation lengths for the 8-nm MnPS_3 device and the 27-nm MnPS_3 device, respectively. The temperature dependences of the magnon relaxation lengths for these devices are similar to that measured on the 16-nm MnPS_3 device [Fig. 3(d)].

Figure 4(c) shows the thickness dependence of the magnon relaxation lengths at $T = 2, 5,$ and 10 K, respectively. Clearly, an increase of the magnon relaxation length is

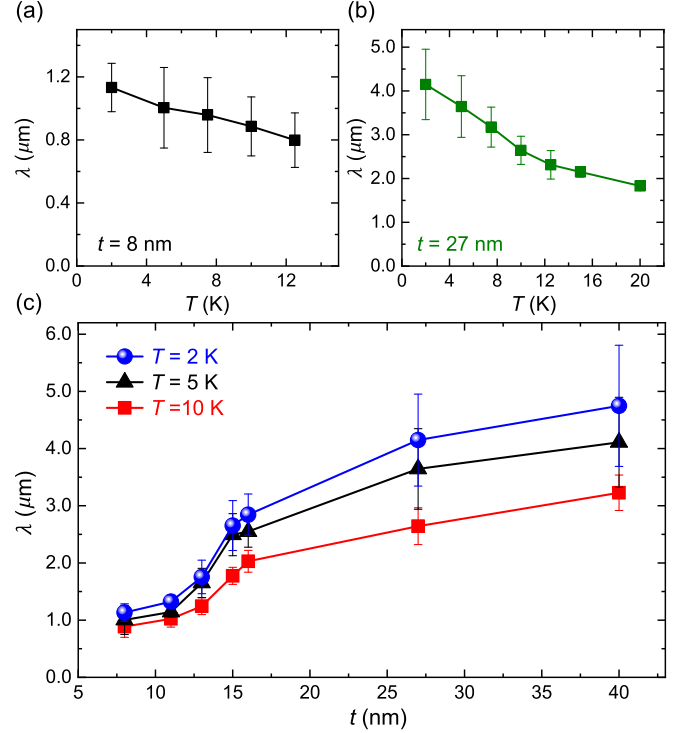


FIG. 4. Thickness dependence of magnon relaxation length of quasi-2D antiferromagnet MnPS_3 . (a),(b) The magnon relaxation length as a function of temperature for the 8- and 27-nm MnPS_3 devices, respectively. (c) The MnPS_3 thickness dependence of the magnon relaxation length obtained at $T = 2, 5,$ and 10 K, respectively.

observed as the 2D MnPS_3 thickness increases and it reaches $\sim 4.7 \mu\text{m}$ for the 40-nm MnPS_3 device. These magnon relaxation lengths for quasi-2D antiferromagnet MnPS_3 are comparable to the values obtained in 3D ferromagnetic insulator YIG [30], which makes quasi-2D antiferromagnet MnPS_3 a promising candidate for magnon spintronics applications. As 2D MnPS_3 thickness decreases, the magnon relaxation length decreases, i.e., a short magnon relaxation length of $\sim 1.1 \mu\text{m}$ is obtained on the 8-nm MnPS_3 device. These results indicate the presence of the enhanced magnon scattering for thinner MnPS_3 . One possible reason is the increase of surface-impurity-induced magnon scattering for thinner MnPS_3 films, which gives rise to the strong suppression of the magnon lifetime. For devices fabricated on ultrathin MnPS_3 flakes, no clear magnon transport signals have been observed yet (see Supplemental Material, Fig. S11 [39] for the results from two typical devices on 5-nm and 4-nm MnPS_3 with $d = 2 \mu\text{m}$), which could be attributed to the presence of strong surface-impurity-induced magnon scattering and lower Néel temperature for thinner MnPS_3 , a Heisenberg antiferromagnet [46].

IV. CONCLUSIONS

In conclusion, long-distance magnon transport over several micrometers has been demonstrated in the

quasi-two-dimensional van der Waals antiferromagnet MnPS_3 . Systematical studies on the temperature and MnPS_3 thickness dependences of the magnon relaxation lengths have been performed. As the 2D MnPS_3 thickness decreases, a shorter magnon diffusion length is observed, which could be attributed to the surface-impurity-induced magnon scattering. Our results demonstrate that van der Waals antiferromagnets provide a 2D platform for magnon spintronics and magnon spin computing [29]. Furthermore, these results could pave the way for the future investigation of novel magnon phenomena in van der Waals 2D magnets, including spin Nernst effect, magnon topological properties, quantum magnon Hall effect, etc. [33–35,37].

ACKNOWLEDGMENTS

We acknowledge the financial support from National Basic Research Programs of China (973 program Grants No. 2015CB921104, No. 2018YFA0305601, and No. 2015CB921102), National Natural Science Foundation of China (NSFC Grants No. 11574006, No. 11774007, No. 11534001, and No. U1832214) and the Strategic Priority Research Program of the Chinese Academy of Sciences (Grant No. XDB28020100).

-
- [1] C. Gong, L. Li, Z. Li, H. Ji, A. Stern, Y. Xia, T. Cao, W. Bao, C. Wang, Y. Wang, Z. Q. Qiu, R. J. Cava, S. G. Louie, J. Xia, and X. Zhang, *Discovery of Intrinsic Ferromagnetism in Two-Dimensional van der Waals Crystals*, *Nature (London)* **546**, 265 (2017).
- [2] B. Huang, G. Clark, E. Navarro-Moratalla, D. R. Klein, R. Cheng, K. L. Seyler, D. Zhong, E. Schmidgall, M. A. McGuire, D. H. Cobden, W. Yao, D. Xiao, P. Jarillo-Herrero, and X. Xu, *Layer-Dependent Ferromagnetism in a van der Waals Crystal down to the Monolayer Limit*, *Nature (London)* **546**, 270 (2017).
- [3] W. Xing, Y. Chen, P. M. Odenthal, X. Zhang, W. Yuan, T. Su, Q. Song, T. Wang, J. Zhong, S. Jia, X. C. Xie, Y. Li, and W. Han, *Electric Field Effect in Multilayer $\text{Cr}_2\text{Ge}_2\text{Te}_6$: A Ferromagnetic 2D Material*, *2D Mater.* **4**, 024009 (2017).
- [4] J.-U. Lee, S. Lee, J. H. Ryoo, S. Kang, T. Y. Kim, P. Kim, C.-H. Park, J.-G. Park, and H. Cheong, *Ising-Type Magnetic Ordering in Atomically Thin FePS_3* , *Nano Lett.* **16**, 7433 (2016).
- [5] X. Wang, K. Du, Y. Y. F. Liu, P. Hu, J. Zhang, Q. Zhang, M. H. S. Owen, X. Lu, C. K. Gan, P. Sengupta, C. Kloc, and Q. Xiong, *Raman Spectroscopy of Atomically Thin Two-Dimensional Magnetic Iron Phosphorus Trisulfide (FePS_3) Crystals*, *2D Mater.* **3**, 031009 (2016).
- [6] N. Samarth, *Condensed-Matter Physics: Magnetism in Flatland*, *Nature (London)* **546**, 216 (2017).
- [7] S. Liu, X. Yuan, Y. Zou, Y. Sheng, C. Huang, E. Zhang, J. Ling, Y. Liu, W. Wang, C. Zhang, J. Zou, K. Wang, and F. Xiu, *Wafer-Scale Two-Dimensional Ferromagnetic Fe_3GeTe_2 Thin Films Grown by Molecular Beam Epitaxy*, *npj 2D Mater. Appl.* **1**, 30 (2017).
- [8] M. Bonilla, S. Kolekar, Y. Ma, H. C. Diaz, V. Kalappattil, R. Das, T. Eggers, H. R. Gutierrez, M.-H. Phan, and M. Batzill, *Strong Room-Temperature Ferromagnetism in VSe_2 Monolayers on van der Waals Substrates*, *Nat. Nanotechnol.* **13**, 289 (2018).
- [9] D. J. O'Hara, T. Zhu, A. H. Trout, A. S. Ahmed, Y. (Kelly) Luo, C. H. Lee, M. R. Brenner, S. Rajan, J. A. Gupta, D. W. McComb, and R. K. Kawakami, *Room Temperature Intrinsic Ferromagnetism in Epitaxial Manganese Selenide Films in the Monolayer Limit*, *Nano Lett.* **18**, 3125 (2018).
- [10] Y. Tian, M. J. Gray, H. Ji, R. J. Cava, and K. S. Burch, *Magneto-Elastic Coupling in a Potential Ferromagnetic 2D Atomic Crystal*, *2D Mater.* **3**, 025035 (2016).
- [11] D. Weber, L. M. Schoop, V. Duppel, J. M. Lippmann, J. Nuss, and B. V. Lotsch, *Magnetic Properties of Restacked 2D Spin 1/2 Honeycomb RuCl_3 Nanosheets*, *Nano Lett.* **16**, 3578 (2016).
- [12] B. Zhou, Y. Wang, G. B. Osterhoudt, P. Lampen-Kelley, D. Mandrus, R. He, K. S. Burch, and E. A. Henriksen, *Possible Structural Transformation and Enhanced Magnetic Fluctuations in Exfoliated α - RuCl_3* , *J. Phys. Chem. Solids*, DOI: 10.1016/j.jpcs.2018.01.026.
- [13] M. Ziatdinov, A. Banerjee, A. Maksov, T. Berlijn, W. Zhou, H. B. Cao, J. Q. Yan, C. A. Bridges, D. G. Mandrus, S. E. Nagler, A. P. Baddorf, and S. V. Kalinin, *Atomic-Scale Observation of Structural and Electronic Orders in the Layered Compound α - RuCl_3* , *Nat. Commun.* **7**, 13774 (2016).
- [14] S. Mashhadi, D. Weber, L. M. Schoop, A. Schulz, B. V. Lotsch, M. Burghard, and K. Kern, *Electrical Transport Signature of the Magnetic Fluctuation-Structure Relation in α - RuCl_3 Nanoflakes*, *Nano Lett.* **18**, 3203 (2018).
- [15] K. S. Burch, D. Mandrus, and J.-G. Park, *Magnetism in Two-Dimensional van der Waals Materials*, *Nature (London)* **563**, 47 (2018).
- [16] N. D. Mermin and H. Wagner, *Absence of Ferromagnetism or Antiferromagnetism in One- or Two-Dimensional Isotropic Heisenberg Models*, *Phys. Rev. Lett.* **17**, 1133 (1966).
- [17] D. R. Klein, D. MacNeill, J. L. Lado, D. Soriano, E. Navarro-Moratalla, K. Watanabe, T. Taniguchi, S. Manni, P. Canfield, J. Fernández-Rossier, and P. Jarillo-Herrero, *Probing Magnetism in 2D van der Waals Crystalline Insulators via Electron Tunneling*, *Science* **360**, 1218 (2018).
- [18] T. Song, X. Cai, M. W.-Y. Tu, X. Zhang, B. Huang, N. P. Wilson, K. L. Seyler, L. Zhu, T. Taniguchi, K. Watanabe, M. A. McGuire, D. H. Cobden, D. Xiao, W. Yao, and X. Xu, *Giant Tunneling Magnetoresistance in Spin-Filter van der Waals Heterostructures*, *Science* **360**, 1214 (2018).
- [19] Z. Wang, I. Gutiérrez-Lezama, N. Ubrig, M. Kroner, T. Taniguchi, K. Watanabe, A. Imamoğlu, E. Giannini, and A. F. Morpurgo, *Very Large Tunneling Magnetoresistance in Layered Magnetic Semiconductor CrI_3* , *Nat. Commun.* **9**, 2516 (2018).
- [20] S. S. P. Parkin, C. Kaiser, A. Panchula, P. M. Rice, B. Hughes, M. Samant, and S.-H. Yang, *Giant Tunneling Magnetoresistance at Room Temperature with MgO (100) Tunnel Barriers*, *Nat. Mater.* **3**, 862 (2004).
- [21] S. Yuasa, T. Nagahama, A. Fukushima, Y. Suzuki, and K. Ando, *Giant Room-Temperature Magnetoresistance in*

- Single-Crystal Fe/MgO/Fe Magnetic Tunnel Junctions*, *Nat. Mater.* **3**, 868 (2004).
- [22] D. Ghazaryan, M. T. Greenaway, Z. Wang, V. H. Guarochico-Moreira, I. J. Vera-Marun, J. Yin, Y. Liao, S. V. Morozov, O. Kristanovski, A. I. Lichtenstein, M. I. Katsnelson, F. Withers, A. Mishchenko, L. Eaves, A. K. Geim, K. S. Novoselov, and A. Misra, *Magnon-Assisted Tunnelling in van der Waals Heterostructures Based on CrBr₃*, *Nat. Electron.* **1**, 344 (2018).
- [23] S. Jiang, J. Shan, and K. F. Mak, *Electric-Field Switching of Two-Dimensional van der Waals Magnets*, *Nat. Mater.* **17**, 406 (2018).
- [24] B. Huang, G. Clark, D. R. Klein, D. MacNeill, E. Navarro-Moratalla, K. L. Seyler, N. Wilson, M. A. McGuire, D. H. Cobden, D. Xiao, W. Yao, P. Jarillo-Herrero, and X. Xu, *Electrical Control of 2D Magnetism in Bilayer CrI₃*, *Nat. Nanotechnol.* **13**, 544 (2018).
- [25] Y. Deng, Y. Yu, Y. Song, J. Zhang, N. Z. Wang, Y. Z. Wu, J. Zhu, J. Wang, X. H. Chen, and Y. Zhang, *Gate-Tunable Room-Temperature Ferromagnetism in Two-Dimensional Fe₃GeTe₂*, *Nature (London)* **563**, 94 (2018).
- [26] Z. Wang, T. Zhang, M. Ding, B. Dong, Y. Li, M. Chen, X. Li, J. Huang, H. Wang, X. Zhao, Y. Li, D. Li, C. Jia, L. Sun, H. Guo, Y. Ye, D. Sun, Y. Chen, T. Yang, J. Zhang *et al.*, *Electric-Field Control of Magnetism in a Few-Layered van der Waals Ferromagnetic Semiconductor*, *Nat. Nanotechnol.* **13**, 554 (2018).
- [27] T. Dietl, *A Ten-Year Perspective on Dilute Magnetic Semiconductors and Oxides*, *Nat. Mater.* **9**, 965 (2010).
- [28] T. Dietl and H. Ohno, *Dilute Ferromagnetic Semiconductors: Physics and Spintronic Structures*, *Rev. Mod. Phys.* **86**, 187 (2014).
- [29] A. V. Chumak, V. I. Vasyuchka, A. A. Serga, and B. Hillebrands, *Magnon Spintronics*, *Nat. Phys.* **11**, 453 (2015).
- [30] L. J. Cornelissen, J. Liu, R. A. Duine, J. B. Youssef, and B. J. van Wees, *Long-Distance Transport of Magnon Spin Information in a Magnetic Insulator at Room Temperature*, *Nat. Phys.* **11**, 1022 (2015).
- [31] W. Yuan, Q. Zhu, T. Su, Y. Yao, W. Xing, Y. Chen, Y. Ma, X. Lin, J. Shi, R. Shindou, X. C. Xie, and W. Han, *Experimental Signatures of Spin Superfluid Ground State in Canted Antiferromagnet Cr₂O₃ via Nonlocal Spin Transport*, *Sci. Adv.* **4**, eaat1098 (2018).
- [32] R. Lebrun, A. Ross, S. A. Bender, A. Qaiumzadeh, L. Baldrati, J. Cramer, A. Brataas, R. A. Duine, and M. Kläui, *Tunable Long-Distance Spin Transport in a Crystalline Antiferromagnetic Iron Oxide*, *Nature (London)* **561**, 222 (2018).
- [33] R. Cheng, S. Okamoto, and D. Xiao, *Spin Nernst Effect of Magnons in Collinear Antiferromagnets*, *Phys. Rev. Lett.* **117**, 217202 (2016).
- [34] K. Nakata, S. K. Kim, J. Klinovaja, and D. Loss, *Magnonic Topological Insulators in Antiferromagnets*, *Phys. Rev. B* **96**, 224414 (2017).
- [35] Y. Su, X. S. Wang, and X. R. Wang, *Magnonic Weyl Semimetal and Chiral Anomaly in Pyrochlore Ferromagnets*, *Phys. Rev. B* **95**, 224403 (2017).
- [36] J. Lan, W. Yu, and J. Xiao, *Antiferromagnetic Domain Wall as Spin Wave Polarizer and Retarder*, *Nat. Commun.* **8**, 178 (2017).
- [37] B. Xu, T. Ohtsuki, and R. Shindou, *Integer Quantum Magnon Hall Plateau-Plateau Transition in a Spin-Ice Model*, *Phys. Rev. B* **94**, 220403 (2016).
- [38] K. Okuda, K. Kurosawa, S. Saito, M. Honda, Z. Yu, and M. Date, *Magnetic Properties of Layered Compound MnPS₃*, *J. Phys. Soc. Jpn.* **55**, 4456 (1986).
- [39] See Supplemental Material at <http://link.aps.org/supplemental/10.1103/PhysRevX.9.011026> for the determination of Néel temperature, atomic force microscopy measurement, Raman characterization, the first and second harmonic nonlocal results, the current dependence of the second harmonic voltage, the insulating properties of quasi-2D MnPS₃, nonlocal measurements on control devices, local vs nonlocal measurements, spacing dependence on extra devices with much larger spacings, and magnon transport in ultrathin 2D MnPS₃ devices.
- [40] S. T. B. Goennenwein, R. Schlitz, M. Pernpeintner, K. Ganzhorn, M. Althammer, R. Gross, and H. Huebl, *Non-Local Magnetoresistance in YIG/Pt Nanostructures*, *Appl. Phys. Lett.* **107**, 172405 (2015).
- [41] L. J. Cornelissen, K. J. H. Peters, G. E. W. Bauer, R. A. Duine, and B. J. van Wees, *Magnon Spin Transport Driven by the Magnon Chemical Potential in a Magnetic Insulator*, *Phys. Rev. B* **94**, 014412 (2016).
- [42] L. J. Cornelissen, J. Shan, and B. J. van Wees, *Temperature Dependence of the Magnon Spin Diffusion Length and Magnon Spin Conductivity in the Magnetic Insulator Yttrium Iron Garnet*, *Phys. Rev. B* **94**, 180402 (2016).
- [43] J. Shan, L. J. Cornelissen, J. Liu, J. B. Youssef, L. Liang, and B. J. van Wees, *Criteria for Accurate Determination of the Magnon Relaxation Length from the Nonlocal Spin Seebeck Effect*, *Phys. Rev. B* **96**, 184427 (2017).
- [44] B. L. Giles, Z. Yang, J. S. Jamison, and R. C. Myers, *Long-Range Pure Magnon Spin Diffusion Observed in a Nonlocal Spin-Seebeck Geometry*, *Phys. Rev. B* **92**, 224415 (2015).
- [45] C. Safranski, I. Barsukov, H. K. Lee, T. Schneider, A. A. Jara, A. Smith, H. Chang, K. Lenz, J. Lindner, Y. Tserkovnyak, M. Wu, and I. N. Krivorotov, *Spin Caloritronic Nano-oscillator*, *Nat. Commun.* **8**, 117 (2017).
- [46] P. A. Joy and S. Vasudevan, *Magnetism in the Layered Transition-Metal Thiophosphates MPS₃ (M = Mn, Fe, and Ni)*, *Phys. Rev. B* **46**, 5425 (1992).
- [47] T. Jungwirth, X. Marti, P. Wadley, and J. Wunderlich, *Antiferromagnetic Spintronics*, *Nat. Nanotechnol.* **11**, 231 (2016).
- [48] V. Baltz, A. Manchon, M. Tsoi, T. Moriyama, T. Ono, and Y. Tserkovnyak, *Antiferromagnetic Spintronics*, *Rev. Mod. Phys.* **90**, 015005 (2018).
- [49] T. Valet and A. Fert, *Theory of the Perpendicular Magnetoresistance in Magnetic Multilayers*, *Phys. Rev. B* **48**, 7099 (1993).
- [50] Y. Shiomi, R. Takashima, D. Okuyama, G. Gitgeatpong, P. Piyawongwatthana, K. Matan, T. J. Sato, and E. Saitoh, *Spin Seebeck Effect in the Polar Antiferromagnet α -Cu₂V₂O₇*, *Phys. Rev. B* **96**, 180414 (2017).
- [51] S. M. Wu, W. Zhang, A. Kc, P. Borisov, J. E. Pearson, J. S. Jiang, D. Lederman, A. Hoffmann, and A. Bhattacharya, *Antiferromagnetic Spin Seebeck Effect*, *Phys. Rev. Lett.* **116**, 097204 (2016).